Catalysis Science & Technology

Accepted Manuscript

ROYAL SOCIETY OF CHEMISTRY

www.rsc.org/catalysis

Catalysis Science & Technology

ARTICLE

Transition metal pairs on ceria-promoted, ordered mesoporous alumina as catalyst for methane-CO_2 reforming reaction

Received 00th January 20xx,
Accepted 00th January 20xx

DOI: 10.1039/x0xx00000x

www.rsc.org/

M. S. Aw[a], G. Dražić[b], P. Djinović[a*] and A. Pintar[a]

CoFe, CoW, N iFe and NiW bimetallic pairs deposited over the CeO_2-ZrO_2 promoted ordered mesoporous γ-Al_2O_3, were tested in methane dry reforming reaction. Catalysts were characterized by N_2 adsorption, wide and small angle XRD, TEM, UV-Vis DRS and H_2-TPR techniques. Upon thermal treatment, diffusion of Ni and Co into the alumina matrix occurred, resulting in the formation of corresponding aluminate spinels. Based on UV-Vis characterization, formation of bulk Fe_2O_3 could be only tentatively assigned in NiFe/AlCZ catalyst. Bulk Co_3O_4 is likely present in both CoW and CoFe catalysts. The CoFe/AlCZ and NiFe/AlCZ catalysts achieved high and stable methane conversion rates of 8.8 and 6.0 mmol CH_4/(g_{cat} min), respectively. Activity of tungsten containing catalysts (CoW/AlCZ and NiW/AlCZ) was substantially lower, compared to iron containing catalysts (2.8 and 0.8 mmol CH_4/(g_{cat} min), respectively) and their deactivation was likely related to sintering and oxidation of active metal clusters. Low carbon content was accumulated on the surface of spent NiFe/AlCZ, CoFe/AlCZ and NiW/AlCZ catalysts after 20 h tests (0.6-1.2 wt. %), indicating high efficiency of the redox promoter under dry reforming conditions.

Introduction

The rapidly diminishing fossil fuel reserves are a critical issue that requires an urgent need to explore sustainable alternatives for power generation and synthesis of chemicals. Producing syngas from renewable resources and industrial flue gases is worthwhile since CH_4 and CO_2 are abundant and available in biogas, whereas CO_2 can also be sourced from oil refineries and thermal power plants.[1] Biogas is an attractive source for renewable CH_4 and CO_2 and is produced by anaerobic digestion of numerous organic materials.[2] Methane and CO_2 can be directly valorised to syngas through methane dry reforming (MDR) reaction. Compared with partial oxidation and steam reforming, MDR produces syngas with a lower H_2/CO stoichiometry that is a valuable chemical feedstock for the production of dimethyl ether (DME),[3] higher alcohols,[4] Fischer–Tropsch synthesis,[5] as well as for downstream processes (carbonylation, hydroformylation).[6] However, the main obstacle preventing stable catalytic performance in methane dry reforming reaction is due to a high thermodynamic driving force for carbon formation in the absence of co-fed oxidant, such as oxygen or water. Transition metal catalysts, especially Ni and Co, are highly active. However, high activity of Ni in methane cracking reaction is known to promote coking,[7] whereas Co is susceptible to oxidation and deactivation.[8] Noble metals are highly active and provide excellent resistance to carbon accumulation, but are unacceptable from an economic aspect.

Hence, notable efforts are focused on developing transition metal catalyst formulations enabling high and stable activity with considerably improved resistance to carbon formation. Literature reports several strategies for the design of stable reforming catalysts, for instance, the use of redox and basic promoters, such as Ni-based catalysts over alumina, alumina-ceria, alumina-magnesia or other alkaline earth supports,[9] formation of atomically dispersed nickel species as present in spinels and hexaaluminates[10] and spatial segregation of active metal clusters via synthesis of core-shell catalyst structures.[11] In our previous work, we demonstrated that a CeO_2-ZrO_2 promoted γ-Al_2O_3 is a highly promising support, in which alumina provides structural rigidity and mechanical stability, while its large surface area and pore volume favour high dispersion of active transition metal clusters. Ceria as a reducible oxide exhibits high mobility of oxygen species that enable on-time gasification of carbon deposits. Zirconia serves as a dopant for ceria and induces lattice strain and defects to promote higher oxygen mobility and thermal stability of ceria. These features, along with an appropriate loading of nanosized NiCo clusters that exhibit reduced metal ensemble size due to alloying and dilution effect,[12] have given rise to remarkably stable catalytic performance and negligible amount of carbonaceous deposits on the extended time scale of 550 h TOS.[12,13]

[a] Laboratory for Environmental Sciences and Engineering
National Institute of Chemistry
Hajdrihova 19, SI-1001 Ljubljana, Slovenia.
[b] Laboratory for Materials Chemistry
National Institute of Chemistry
Hajdrihova 19, SI-1001 Ljubljana, Slovenia.

*e-mail: petar.djinovic@ki.si
Electronic Supplementary Information (ESI) available: DOI: 10.1039/x0xx00000x

In the present study, we explore the possibility to expand and generalize the bimetallic transition metal catalyst approach for stable and selective methane-CO_2 reforming reaction. Several functionalities were incorporated into the designed materials in order to reach this goal:

Ordered mesoporous γ-Al_2O_3 with uniform hexagonal arrays of parallel cylindrical pores was employed to support and spatially separate active metal clusters inside its pores in order to prevent their sintering and agglomeration, thereby maintaining high dispersion.[14]

A second transition metal (Fe or W) was paired with either Ni or Co. Both Fe and W possess multiple oxidation states which are capable of improving the redox properties of Ni or Co metallic clusters.[15] Fast transition between oxidation states is crucial as the surface oxygen atoms of Fe and W can act as local oxygen sources for continuous removal of carbonaceous deposits. Moreover, catalytic activity of bi-metallic clusters can be enhanced due to the variable local atom coordination and co-existence of bimetallic junctions that govern the electronic properties of catalysts.[15]

The role of ceria-zirconia redox promoter is to supply oxygen species to the active metal cluster-support interface, which facilitates carbon gasification.[12]

In this work, the multifunctional bimetallic transition metal catalysts were thoroughly characterized and their performance in methane dry reforming reaction systematically examined.

Experimental

Ordered mesoporous alumina (Al) was prepared by means of evaporation-induced self-assembly method.[14] 1 g of Pluronic® P123, Mw = 5800, was dissolved in 20 mL of anhydrous ethanol under stirring. Separately, 2 g of aluminium isopropoxide was dissolved in 1.67 mL of 67 % nitric acid and 16.7 mL of anhydrous ethanol and stirred vigorously for 1 h. The two solutions were combined and stirred vigorously for another 5 h. The gel was poured into a Petri dish and oven-dried at 60 °C for 48 h. The dried sample was calcined in a chamber oven in static air. Temperature was raised (2 °C/min) from ambient to 600 °C, followed by further heating (2 °C/min) to 800 °C. Isothermal steps were maintained for 2 h each.

The 6 wt. % of ceria-zirconia (CZ) (wt. ratio of Ce:Zr = 4:1) was wet impregnated over the Al support. The suspension was mixed overnight, filtered and oven-dried at 100 °C for 24 h, followed by calcination at 350 °C for 4 h. The obtained product was ground to fine powdered form (denoted as AlCZ).

Nitrate precursors of Ni, Co, Fe, and ammonium metatungstate hydrate were wet-impregnated onto the AlCZ. The wt. ratio of Ni or Co to Fe or W equal to 1 to 4 was used, and a total of 3 wt. % metal loading was deposited during overnight stirring. Obtained powders were oven dried at 100 °C for 24 h and calcined in air at 650 °C for 4 h. The prepared samples are denoted as NiFe/AlCZ, NiW/AlCZ, CoFe/AlCZ and CoW/AlCZ, respectively. Chemical composition of synthesized materials was analyzed according to ISO 17294-2 standard using ICP MS technique; the obtained results are provided in supplementary information (Table S1).

The N_2 adsorption was performed using the Micromeritics TriStar II 3020 apparatus. Prior to analysis, the samples were degassed in N_2 flow for 1 h at 90 °C, followed by 4 h at 180 °C using the Micromeritics SmartPrep Degasser. Pore size distribution was obtained from N_2 desorption branch of the isotherm using the BJH method and total pore volumes from volume adsorbed at relative pressures close to 0.995.

Powdered X-ray diffraction (XRD) analysis was performed using an X'pert Pro diffractometer by PANalytical using CuKα1 radiation (λ = 0.15406 nm) with a 0.016° (small angle) and 0.032° (wide angle) step size. In both cases, scan speed was 100 s per step.

Transmission electron microscopy (TEM) and energy-dispersive x-ray spectroscopy (EDXS) were conducted to image the samples. Specimens were ultrasonically dispersed in ethanol and deposited on a copper grid covered with a carbon film prior to analysis. The JEOL ARM 200 CF scanning transmission electron microscope with atomic resolution, equipped with a cold field-emission gun, probe spherical aberration corrector (CESCOR unit from CEOS, Germany) and Jeol Centurio EDXS system with 100 mm^2 SDD detector, was used to examine the selected AlCZ support, CoFe/AlCZ, NiW/AlCZ and NiFe/AlCZ catalysts.

Deposited carbon amount was quantified over spent catalysts by means of CHNS elemental analysis (2400 series II analyzer by Perkin Elmer).

Temperature programmed reduction (H_2-TPR) was performed to determine the redox behaviour and oxygen storage capacity of prepared catalysts (AutoChem II 2920 apparatus by Micromeritics). Prior to analysis, the samples were pre-treated at 300 °C in synthetic air for 60 min, followed by cooling to 20 °C in Ar. After 15 min, the flow was changed to 5 % H_2/Ar and a linear temperature ramp of 10 °C/min was employed until reaching the final temperature of 850 °C.

UV-Vis diffuse-reflectance spectroscopic characterization (UV-Vis DRS) was performed using a Lambda 650 spectrophotometer by Perkin Elmer, equipped with a praying mantis accessory for measuring the powdered samples and SPECTRALON™ as the background.

Activity tests of the prepared catalysts in MDR were performed in a Microactivity Reference reactor system (PID Eng&Tech) at 750 °C and 1.2 bar which lasted for 20 h. 200 mg of a catalyst was diluted with 1133 mg SiC to form the catalytic bed, sandwiched between two flocks of quartz wool and positioned in the tubular quartz reactor (I.D. = 10 mm). Temperature was measured using a K-type thermocouple, placed at the centre of the catalyst bed. The catalyst was reduced *in-situ* prior to tests at 750 °C for 1 h in a 20 % H_2/N_2 flow of 50 NmL/min. Equimolar reactant feed of CH_4 and CO_2 (50 NmL/min each) was fed into the reactor. Gases leaving the reactor were analyzed using a gas chromatograph (Agilent Technologies, model 7890A), equipped with Poraplot Q and Molesieve 5A capillary columns.

Results and discussion

Textural properties

Table 1 shows textural properties of prepared materials. BET specific surface area, total pore volume and average pore diameter of ordered mesoporous Al support correspond closely to the expected values.[14] Upon subsequent deposition of CZ, these properties were not affected, besides minor decrease of the average pore diameter. This implies that the introduction of 6 wt. % CeO_2 and ZrO_2 caused no pore blockage or structural modifications of the Al support (see also Figs. S1 and S2).

BET specific surface area and total pore volume values of the catalysts were found to decrease by 13-33 % (Table 1) upon deposition of active metals. This was associated also with an observed increase of the average pore diameter. It is likely that calcination at 650 °C, which was employed after the metal deposition, resulted in structural changes of solids.

N_2 adsorption/desorption isotherms (Fig. S1) obtained over the synthesized materials, exhibit type-IV isotherm with H1-type hysteresis loop, usually found in highly ordered MCM-41 and SBA-15 siliceous materials containing uniform and parallel cylindrical pores.[16] For all materials, the capillary condensation step occurred steeply in the P/P_o range between 0.7 and 0.9, indicating that the contribution from structural porosity (interparticle porosity) is minor and most of the adsorption has occurred within the ordered cylindrical pores.

Table 1. Textural properties of synthesized materials prior to catalytic runs.

Sample	BET specific surface area (m^2/g)	Total pore volume (cm^3/g)	Average pore diameter (nm)
Al	295	0.78	8.3
AlCZ	294	0.76	7.9
NiFe/AlCZ	184	0.45	9.8
NiW/AlCZ	228	0.50	10.5
CoFe/AlCZ	256	0.57	10.0
CoW/AlCZ	220	0.49	13.5

XRD examination

XRD patterns of calcined alumina materials after CZ promotion and deposition of active phases are presented in Fig. 1. XRD pattern of promoted AlCZ support containing 6 wt. % CeO_2 and ZrO_2 is dominated by CeO_2 peaks at 2theta values of 28.9, 33.3, 48.4, 57.3, 70.6 and 78.1° (PDF entry 34-0394). The calculated CeO_2 crystallite size based on the most intense reflection at 28.9° using Scherrer's equation, was 5.3 nm.

The diffraction patterns of γ-Al_2O_3 phase (PDF entry 13-0373) at 2theta values of 37.3, 46.3 and 67° became apparent after active metal deposition and calcination, suggesting low crystallinity and/or small sizes of coherently scattering domains in the promoted mesoporous alumina support.

Presence of active metal pairs (3 wt. % of NiFe, NiW, CoFe or CoW) produced additional reflections with low intensity that could be ascribed to NiO, Co_3O_4 and Fe_2O_3. Introduction of the bimetallic pairs (especially Ni and Fe), followed by thermal treatment resulted also in appearance of broad reflections which could be ascribed to $NiAl_2O_4$ and $Al_3Fe_5O_{12}$ spinel phases. Presence of any tungsten containing crystalline phases could not be identified using this technique probably due to its tendency for forming WO_x oligomeric and polymeric species instead of crystalline nanoclusters at low tungsten loadings.[17]

Small-angle XRD analysis was performed to identify mesoscopic order of synthesized materials (Fig. 1, inset). Reflections for Al support observed at 0.98 and 1.58° can be ascribed to diffraction from (100) and (110) planes, related to its ordered mesoporous hexagonal structure with p6mm symmetry.[18] After CZ deposition, the intensity of the (100) peak was maintained, while reflection from the (110) plane disappeared. Relative peak intensities are known to depend on the ratio of the pore diameter to the pore wall thickness and on the type of periodic voids in the structure.[19] These factors contributed to the observed alteration of the SAXS profile, which is in line with the results of N_2 adsorption, as total pore volume and pore diameter was seen to decrease by 0.02 cm^3/g and 0.4 nm, respectively. This indicates that the incorporation of 6 wt. % CZ did not disrupt the 2D hexagonal ordered pore structure of AlCZ support.

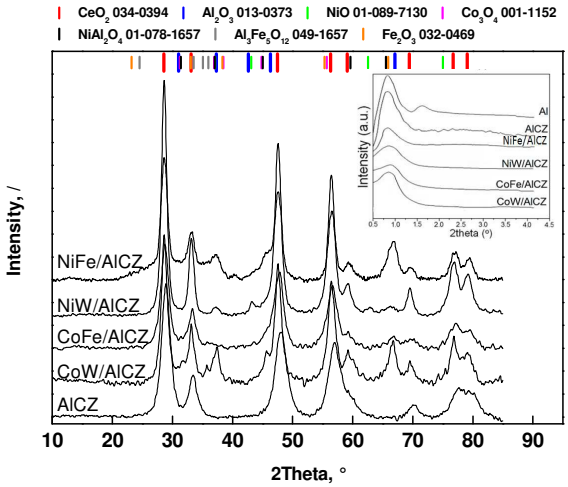

Figure 1. Wide-angle XRD diffractograms for AlCZ support and NiFe/AlCZ, NiW/AlCZ, CoFe/AlCZ and CoW/AlCZ catalysts. Inset: small-angle XRD diffractograms for all supports and catalysts.

After deposition of Ni, Co, Fe or W, SAXS profiles were considerably suppressed in intensity and only diffraction from (100) plane was present. This was accompanied with a considerable loss of BET specific surface area and total pore volume. Also, average pore diameter was found to increase (Table 1), which is indicative of some loss of their mesoscopic order.

TEM-EDXS analysis

TEM images of Al and AlCZ supports (Fig. 2a and b) show their ordered mesoporous morphology and presence of parallel cylindrical pores.

After deposition of active metal pairs, the mesoscopic order was largely maintained (Fig. 2c and 2d showing NiW and NiFe containing catalysts). In addition to ordered regions, areas of irregular morphology were also observed (Fig. S3a and S3b), likely as a result of calcination (4 h at 650 °C) and reduction (1

h at 500 °C) after active metal deposition. This is in accordance with N_2 adsorption data (Table 1), which indicated some deviation from the parent morphology of AlCZ support.

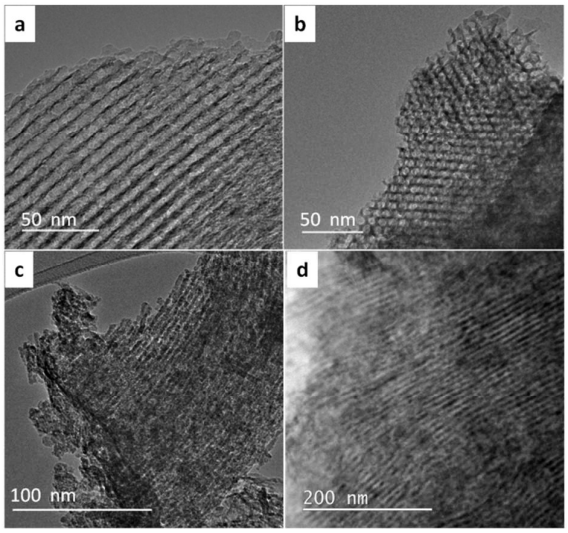

Figure 2. TEM images of: a) Al support viewed perpendicular to the pores, b) CZ promoted Al support viewed parallel with the pores, c) NiW/AlCZ and d) NiFe/AlCZ catalysts.

Distribution of active components over the Al support was investigated using ABF-STEM, HAADF-STEM and EDXS analysis (Fig. 3 and Fig. S3).

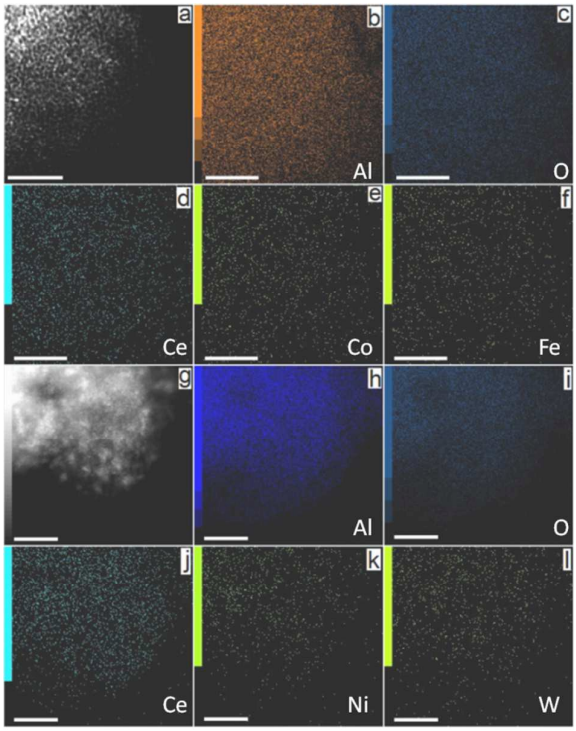

Figure 3. HAADF-STEM images of CoFe/AlCZ sample with EDXS elemental mapping (a-f, scale bar = 100 nm) and NiW/AlCZ sample with EDXS elemental mapping (g-l, scale bar = 5 nm).

Annular dark field scanning TEM images (HAADF-STEM) of CoFe/AlCZ and NiW/AlCZ catalysts (Fig. 3a and 3g) with corresponding EDXS elemental mapping revealed the presence of isolated single atom or several atom clusters of active metals and CeO_x redox promoter over the Al support in the examined materials. Considering that both UV-Vis DRS and XRD analyses suggest formation of Ni and Co aluminate spinel structures, these observed species are likely incorporated into the Al support.

Besides homogeneously dispersed single/several atom clusters (Figs. S3c, S3f, S3g and S3h), areas where active phase confinement within the cylindrical pores of the support occurred, were also observed (Figs. S3d and S3e). This explains the origin of dominating XRD reflections belonging to CeO_2 in the synthesized materials. In addition, active metal clusters between 1 and 3 nm in size were also observed (Fig. S3i). Briefly, active catalytic components in the analyzed catalysts were identified as highly polydispersed over the alumina support.

UV-Vis DRS examination

UV-Vis DRS absorption spectra of bimetallic catalysts and Al support prior/after CZ promotion are presented in Fig. 4. Spectra are dominated by strong absorption below 400 nm, which is attributed to intrinsic band gap absorption of CeO_2 due to electron transition from valence to conduction band. Two contributions are visible in this range, namely one signal at 241 nm which is characteristic of $O_2 \rightarrow Ce^{3+}$ ligand to metal charge transfer (LMCT) and the second at 297 nm, resulting from $O_2 \rightarrow Ce^{4+}$ LMCT. Weak absorption of Al support in the region below 400 nm is likely a consequence of a small amount of present impurities.

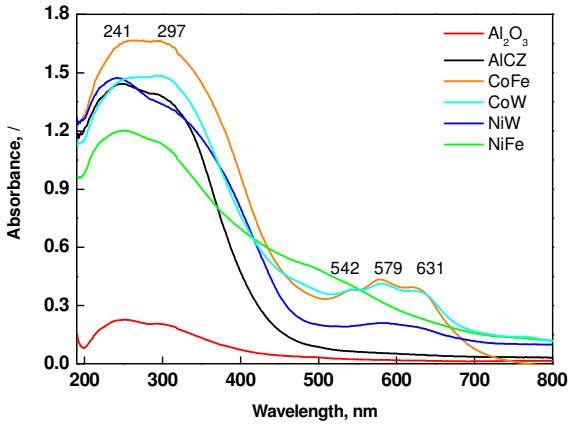

Figure 4. UV-Vis DRS spectra of bimetallic catalysts and Al support prior and after CZ promotion.

Upon deposition of transition metal pairs, additional bands between 400 and 700 nm were observed. Cobalt containing catalysts (CoW and CoFe) both exhibited a characteristic triplet at 542, 579 and 631 nm, which are the Co^{2+} d–d electron transitions and are indicative of Co^{2+} ions in tetrahedral coordination, as present in $CoAl_2O_4$ spinel.[20]

Nickel containing catalysts (NiW and NiFe) exhibited a less intense doublet at 580 and 631 nm, which can be attributed to d-d transition of Ni^{2+} in octahedral coordination, which is characteristic of nickel aluminate spinel.[20] The low intensity of Ni^{2+} d–d bands is consistent with centro-symmetric geometry of this nickel coordination.

The broad shoulder located between 450 and 550 nm is characteristic for $O_2 \rightarrow Fe^{3+}$ LMCT of octahedrally coordinated iron (Fig. S4).[21] This band was most intense in NiFe catalyst, indicating that iron with low dispersion was present in this sample. Also, Co_3O_4 absorbs light in the broad range of wavelengths ($O_2 \rightarrow Co^{2+}$ LMCT between 300-500 nm and $O_2 \rightarrow Co^{3+}$ LMCT between 550-750 nm; see Fig. S4). This would explain presence of a shoulder in the 450-550 nm region of CoW and CoFe samples.

Results of UV-Vis DRS analyses indicate that incorporation of nickel and cobalt into Al support occurred, forming aluminate spinels. Formation of bulk Fe_2O_3 could be only tentatively assigned in NiFe catalyst. Bulk Co_3O_4 is likely present in both CoW and CoFe catalysts.

H_2-TPR measurements

Redox properties of reforming catalysts are known for being crucial in enabling efficient online gasification of carbon deposits by providing oxygen species to the metallic clusters.[22] Recorded H_2-TPR profiles are presented in Fig. 5. Pure ordered mesoporous γ-Al_2O_3 shows no reaction with hydrogen gas at temperatures up to 850 °C. Upon deposition of 6 wt. % CeO_2-ZrO_2 redox promoter, several peaks were observed. Reduction of surface capping Ce^{4+} cations, along with small CeO_2 clusters takes place between 250 and 500 °C, whereas bulk CeO_2 reduction occurred above 650 °C. Formation of a CeO_2–ZrO_2 solid solution results in a downward shift of bulk reduction temperature to about 550–650 °C.[22] The obtained reduction profile of redox promoted Al support is consistent with XRD and TEM-EDX results (Figs. 1, 3 and S3) and confirms the presence of both bulk crystalline CeO_2 as well as finely dispersed CeO_2 clusters.

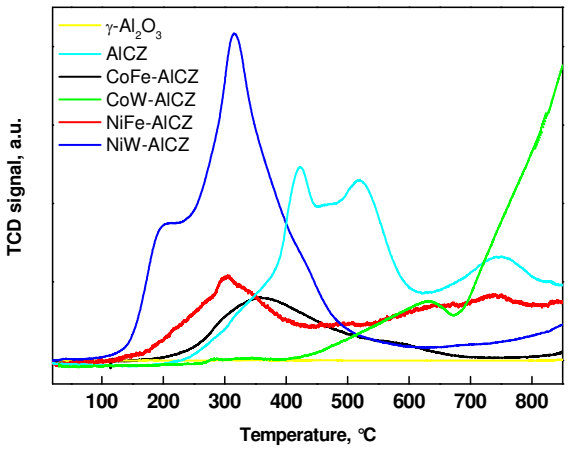

Figure 5. H_2-TPR profiles of bimetallic catalysts and Al support prior and after CZ promotion.

Deposition of transition metal pairs resulted in a substantial alteration of reduction profiles, indicating markedly altered redox properties when all components are present on the catalyst (active transition metal, redox promoter and alumina support). The origin of this phenomenon can lie in the formation of mixed oxide phases, decoration of CeO_2 nanoclusters with transition metal atoms or electronic interactions between the metal cations and redox promoter.

The CoFe, NiFe and especially NiW/AlCZ catalysts exhibited several peaks below 500 °C, indicating facile reduction of transition metal moieties and redox promoter. On the contrary, CoW/AlCZ catalyst exhibited negligible H_2 consumption below 400 °C with a slow rising peak centred at about 620 °C and a large peak extending beyond 850 °C. The first peak corresponds closely (according to its position and quantity of consumed H_2, namely 3.5 mL measured vs. 3.1 mL according to the actual loading of CeO_2) to reduction of CeO_2. The reduction peak at temperatures above 700 °C resembles that of bulk crystalline WO_3 (Fig. S5). These results suggest that redox properties of CoW/AlCZ catalyst become prominent at temperatures which are significantly higher, compared to other tested materials and also higher than the employed reaction temperature, which might indicate its limited functionality in preventing carbon accumulation.

Methane dry reforming

Fig. 6 shows the MDR activity profiles of bimetallic catalysts during 20 h tests.

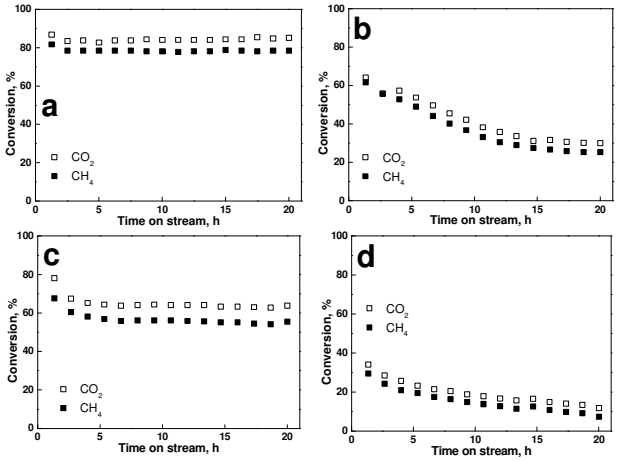

Figure 6. Methane and CO_2 conversion profiles for: a) CoFe/AlCZ, b) CoW/AlCZ, c) NiFe/AlCZ and d) NiW/AlCZ catalysts over 20 h time on stream.

In all four experiments, concentration of produced CO was higher than that of H_2 (Table 2). This clearly demonstrates that MDR occurred concurrently with the reverse water-gas shift (RWGS) reaction. With CoFe/AlCZ and NiFe/AlCZ catalysts, stable activity with no signs of deactivation after 20 h was achieved. It is important to note that cobalt containing catalyst was more active than the nickel containing one, despite the higher intrinsic activity of nickel for C-H bond cleavage, which is generally considered as a rate determining step in methane reforming. Higher activity of cobalt compared to nickel in the

methane dry reforming reaction has been observed also previously when these metals were dispersed over γ-Al_2O_3.[23]

As both cobalt and nickel are, according to UV-Vis DRS characterization, predominantly present as highly dispersed in alumina matrix forming their corresponding spinels, their intrinsic activity may be fundamentally different compared to either cobalt or nickel (nano)crystallites.[24]

In the following paragraph the effect of iron is discussed. Activation of C-H bond in methane proceeds more readily on open crystalline planes of Fe (100) and especially in presence of coordinatively unsaturated surface Fe ad-atoms, compared to more densely packed Fe (110) crystalline plane.[25] As a result, iron clusters composed of several atoms, which contain a high fraction of step and kink atoms, are expected to exhibit considerably higher activity for methane activation, compared to their bulk counterparts. Based on the results of UV-Vis DRS characterization (Fig. 4), CoFe/AlCZ catalyst contains highly dispersed iron clusters, whereas crystalline Fe_2O_3 was identified in NiFe/AlCZ sample. Activity of CoFe/AlCZ catalyst was noticeably higher compared to that of NiFe/AlCZ (8.8 and 6.0 mmol $CH_4/(g_{cat}$ min), respectively), confirming the important role of finely dispersed Fe clusters on enabling high catalytic activity in the methane-CO_2 reforming reaction. These materials notably outperformed also the NiCo/γ-Al_2O_3 bimetallic catalyst, which achieved a methane conversion rate of 3.7 mmol $CH_4/(g_{cat}$ min).[13]

Table 2. Conversion of methane and CO_2, H_2/CO ratio and the amount of accumulated carbon during 20 h MDR tests.

Sample	CH_4 conversion (%)*	CO_2 conversion (%)*	H_2/CO ratio*	Carbon content (wt. %)
NiFe/AlCZ	54	64	0.61	0.6
NiW/AlCZ	7	12	0.31	0.8
CoFe/AlCZ	79	85	0.69	1.2
CoW/AlCZ	25	30	0.35	4.7

*Evaluated at 20 h TOS.

Iron is known (and widely employed) to catalyze the WGS reaction at high temperatures.[26] At the reaction conditions used in this study (T=750 °C, P=1.2 bar, K_{wgs}=1.3), iron nanocrystallites as identified in NiFe/AlCZ catalyst, promoted WGS reaction and caused the lowering of H_2/CO ratio in the produced syngas, in comparison to CoFe/AlCZ sample (Table 2).

In order to more explicitly illustrate the role of redox promotion, experiments with NiFe/Al vs. NiFe/AlCZ and CoFe/Al vs. CoFe/AlCZ were performed. Also, a comparison between corresponding monometallic (3 wt. % Ni/AlCZ, 3 wt. % Co/AlCZ and 3 wt. % Fe/AlCZ) and bimetallic catalysts was carried out. Results are presented in Fig. 7 and are based on the most important parameter, namely ability for suppressing coke accumulation.

When comparing the performance of Ni/AlCZ and NiFe/AlCZ catalysts, the monometallic catalyst exhibited both higher activity (80 vs. 54 % CH_4 conversion) and H_2/CO ratio in the produced syngas (0.80 vs. 0.61 at 20 h TOS, respectively). These results highlight the following findings: (i) by employing a bimetallic catalyst, nickel is diluted with iron and its intrinsic activity for the CH_4-CO_2 reforming reaction is lower; (ii) iron exhibits high WGS activity and the H_2/CO ratio in the produced syngas is decreased due to a more pronounced contribution of WGS reaction to the overall product distribution. However, the amount of accumulated carbon on the monometallic catalyst was substantially higher compared to the bimetallic one (15.2 vs. 0.6 wt. % for Ni/AlCZ and NiFe/AlCZ, respectively). This holds also for cobalt based catalysts (9.0 vs. 1.2 wt. % for Co/AlCZ and CoFe/AlCZ, respectively).

Similarly, carbon accumulation was faster when the catalyst redox function was absent in the bimetallic catalysts (1.6 vs. 0.6 wt. % for NiFe/Al and NiFe/AlCZ; 14.5 vs. 1.2 wt. % for CoFe/Al and CoFe/AlCZ, respectively).

In order to maintain low carbon accumulation, it is of crucial importance that carbon forming reactions (promoted by metals) and carbon gasification reactions (enabled by redox function) are balanced. This can be achieved through metal cluster size control (metal loading, synthesis method, …), metal alloying, enhanced redox property of the support or combinations thereof.[22]

It can be seen that simultaneously employing both metal alloying and redox promotion was the only combination that enabled realization of this goal when using catalysts based on CoFe and NiFe pairs.

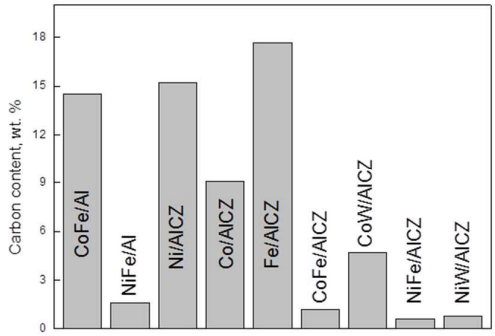

Figure 7. Influence of alloying (monometallic vs. bimetallic) and redox promotion on the accumulated carbon during 20 h time on stream tests.

The initial and final activity of tungsten containing catalysts was lower, when analogous materials are compared (CoFe vs. CoW in Figs. 6a and 6d; NiFe and NiW in Figs. 6b and 6c), indicating important contribution of iron to CH_4-CO_2 reforming activity and especially stability.

Pronounced deactivation was detected for both tungsten containing materials (Fig. 6b and d) with activity of CoW/AlCZ stabilizing after 15 h TOS, while performance of NiW/AlCZ decreased throughout the whole test. If one considers that analogous catalysts with iron as the second metal performed steadily, the deactivation is likely linked to the alteration of morphology (sintering) or chemical state of tungsten, namely oxidation of tungsten species.[27] The role of carbon accumulation on catalyst deactivation was not prominent, especially since continuous deactivation of NiW/AlCZ catalyst was accompanied by a low amount of carbon deposits. It is

known that both active and inactive carbon types can be formed on the catalyst surface during methane dry reforming reaction, and especially the former is known not to influence the catalytic activity negatively.[28] However, carbon accumulation reduces the porosity of the catalytic layer, resulting in an increasing pressure drop across the reactor. The CoW/AlCZ catalyst contained a four to eight fold higher amount of carbon compared to other catalysts (Table 2). Considering that its ability to release oxygen lights off at temperatures above 700 °C, it is likely that oxidation of carbon deposits was lagging, resulting in its faster accumulation compared to other materials which exhibited significant reduction at considerably lower temperatures (Fig. 5).

In order to probe acid sites of the tested catalysts and their possible role in the accumulation of carbon, pyridine TPD was employed (for experimental details please refer to Supporting information). The CoFe/AlCZ, NiW/AlCZ and NiFe/AlCZ catalysts exhibited the highest number of acid sites (Fig. S6, 0.54-0.61 mmol/g_{cat}) and accumulated between 0.6 and 1.2 wt. % of carbon during the catalytic runs.

The number of acid sites over CoW/AlCZ catalyst was substantially lower (0.14 mmol/g_{cat}). However, the amount of coke was the highest over this sample (4.7 wt. %). Based on the lack of correlation between catalyst acidity and amount of accumulated coke, we can conclude that coke accumulation during the methane-CO_2 reforming reaction is not predominantly associated with presence of acid sites, but rather with morphology of active metal clusters and especially redox properties of the promoted support.

Syngas produced by CoW/AlCZ and NiW/AlCZ catalysts contained a considerable surplus of CO (H_2/CO ratio between 0.31 and 0.35, Table 2) with a simultaneously increased concentration of produced water. This could originate either from methane oxidation with oxygen species originating from disproportionation of CO_2, or high WGS activity, especially since tungsten is known to promote both of these reactions.[29,30] Exact contribution of each of these reactions is not possible, as they both (in addition to the targeted MDR reaction) contribute to the mixture of identified reaction products.

Based on its highest catalytic activity and stability in the process under consideration, CoFe/AlCZ catalyst was tested for long-term stability (Fig. 8).

The test confirmed no deactivation of this catalyst also on the 250 h time scale. Methane conversion of 80 % was achieved with a H_2/CO ratio of 0.68. These values are within the experimental error, compared to the short term test, presented in Fig. 6a and Table 2. The amounts of carbon accumulated on the catalyst after the 20 h (Table 2) and 250 h test were the same (1.2 wt. %), indicating that in the initial stage of reaction, equilibrium coverage of the catalyst surface with carbon species was reached, which did not change during prolonged time of reaction.

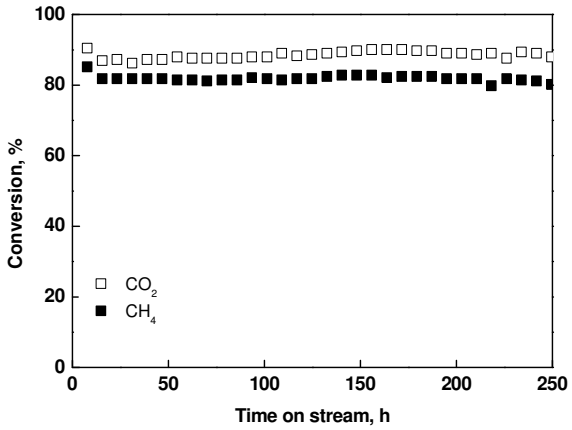

Figure 8. Methane and carbon dioxide conversions during long-term activity test performed in the presence of CoFe/AlCZ catalyst.

TEM examination of the spent CoW/AlCZ catalyst after the 20 h test is shown in Fig. 9.

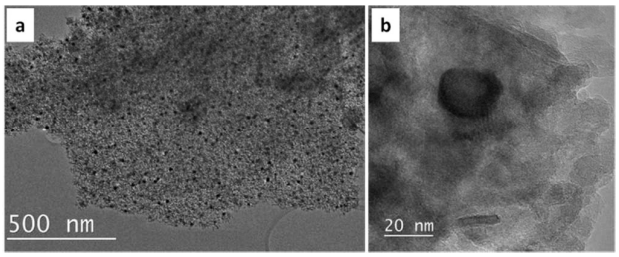

Figure 9. TEM images of the spent CoW/AlCZ catalyst after 20 h TOS reforming reaction: a) catalyst grain containing dispersed metal clusters over the alumina support; b) magnified metal cluster.

Presence of carbon nanofilaments on the catalyst surface could not be identified, despite meticulous analysis of many catalyst grains. Mesoporous order was lost in the spent catalyst as a result of high reaction temperature. Nevertheless, metal clusters were homogeneously dispersed over the support (Fig. 9a), forming polyhedral particles between 20-25 nm in size (Fig. 9b). The CoW/AlCZ catalyst during the 20 h test lost 60 % of initial activity (a decrease from 7.0 to 2.8 mmol CH_4/(g_{cat} min)). Based on the TEM imaging of the spent sample, we can attribute this drop of catalytic activity to sintering of the active metal phases. However, this was not the case when the MDR reaction was conducted in the presence of CoFe/AlCZ catalyst (Fig. 8).

Conclusions

Bimetallic pairs of nickel and iron or cobalt and iron in a 1 to 4 mass ratio, supported over a CeO_2-ZrO_2 promoted ordered mesoporous γ-Al_2O_3, were demonstrated to produce very active and stable catalysts for the reaction of methane reforming with CO_2 over extended time periods.

Prior to catalyst activation in H_2/N_2 stream, active metals (Ni, W, Co, and Fe) as well as redox promoter were identified as single and several atom clusters densely covering the ordered mesoporous γ-Al_2O_3 support. After thermal treatment,

diffusion of Ni and Co into the alumina matrix occurred, resulting in the formation of corresponding aluminate spinels. Based on UV-Vis DRS characterization, formation of bulk Fe_2O_3 could be only tentatively assigned in NiFe catalyst. Bulk Co_3O_4 is likely present in both CoW and CoFe catalysts.

CoFe/AlCZ and NiFe/AlCZ achieved methane conversion rates of 8.8 and 6.0 mmol $CH_4/(g_{cat}$ min), respectively.

Activity of tungsten containing catalysts (CoW and NiW) was substantially lower, compared to iron containing catalysts, namely 2.8 and 0.8 mmol $CH_4/(g_{cat}$ min), respectively, and their deactivation was likely related to sintering or oxidation of active metal clusters. Low carbon content was accumulated on the surface of spent NiFe, CoFe and NiW/AlCZ catalysts after 20 h tests (0.6-1.2 wt. %). These materials exhibited substantial reducibility at temperatures between 100 and 600 °C, highlighting the role of ceria-zirconia redox promoter in preventing carbon accumulation over the bimetallic catalysts.

Acknowledgements

The authors gratefully acknowledge the projects funded by the Ministry of Education, Science and Sport of the Republic of Slovenia through research programs P2-0150 and L2-5465. The financial support for the postdoctoral fellowship (M.S. Aw) offered by the National Institute of Chemistry, Ljubljana, Slovenia, is also gratefully acknowledged.

References

1 S.N. Naik, V.V. Goud, P.K. Rout, A.K. Dalai, Renew. Sust. Energ. Rev. 2010, 14, 578; K. Srirangan, L. Akawi, M. Moo-Young, C.P. Chou, Appl. Energy 2012, 100, 172; A. Mustafa Omer, J. Chem. Mater. Res. 2014, 1, 79.

2 L. Appels, J. Lauwers, J. Degrève, L. Helsen, B. Lievens, K. Willems, J. V. Impe, R. Dewil, Renew. Sust. Energ. Rev. 2011, 15, 4295.

3 Y.C. Lin, L.T. Fan, S. Shafie, B. Bertók, F. Friedler, Comput. Chem. Eng. 2009, 33, 1182; Y. Zhang, S. Zhang, T. Benson, Fuel Process. Technol. 2015, 131, 7; R. Chakrabarti, J.S. Kruger, R.J. Hermann, S.D. Blass, L.D. Schmidt, Appl. Catal. A 2014, 483, 97.

4 M. Gupta, M.L. Smith, J.J. Spivey, ACS Catal. 2011, 1, 641.

5 G. Yang, C. Xing, W. Hirohama, Y. Jin, C. Zeng, Y. Suehiro, T. Wang, Y. Yoneyama, N. Tsubaki, Catal. Today, 2013, 215, 29; A.S. Bambal, V.S. Guggilla, E.L. Kugler, T.H. Gardner, D.B. Dadyburjor, Ind. Eng. Chem. Res. 2014, 53, 5846; M.K. Gnanamani, W.D. Shafer, D.E. Sparks, B.H. Davis, Catal. Commun. 2011, 12, 936.

6 S.H. Christensen, E.P.K. Olsen, J. Rosenbauma, R. Madsen, Org. Biomol. Chem. 2015, 13, 938; G. Makado, T. Morimoto, Y. Sugimoto, K. Tsutsumi, N. Kagawa, K. Kakiuchi, Adv. Synth. Catal. 2010, 352, 299; J.L. Arias, P. Sharma, A. Cabrera, F. Beristain, R. Sampere, C. Arizmendi, Transit. Metal Chem. 2013, 38, 787.

7 A. Djaidja, S. Libs, A. Kiennemann, A. Barama, Catal. Today 2006, 113, 194; J. Guo, H. Lou, H. Zhao, D. Chai, X. Zheng, Appl. Catal. A 2004, 273, 75; F. Frusteri, F. Arena, G. Calogero, T. Torre, A. Parmaliana, Catal. Commun. 2001, 2, 49.

8 P. Djinović, I.G. Osojnik Črnivec, B. Erjavec, A. Pintar, ChemCatChem 2014, 6, 1652.

9 A. Kambolis, H. Matralis, A. Trovarelli, C. Papadopoulou, Appl. Catal. A. 2010, 377, 16; J.W. Thybaut, G.B. Marin, C. Mirodatos, Y. Schuurman, A.C. van Veen, V.A. Sadykov, H. Pennemann, R. Bellinghausen, L. Mleczko, Chem. Ing. Tech. 2014, 86, 1855; E.C. Faria, R.C.R. Neto, R.C. Colman, F.B. Noronha, Catal. Today 2014, 228, 138.

10 R. Benrabaa, A. Löfberg, J.G. Caballero, E. Bordes-Richard, A. Rubbens, R.N. Vannier, H. Boukhlouf, A. Barama, Catal. Commun. 2015, 58, 127; T. Roussière, K.M. Schelkle, S. Titlbach, G. Wasserschaff, A. Milanov, G. Cox, E. Schwab, O. Deutschmann, L. Schulz, A. Jentys, J. Lercher, S.A. Schunk, ChemCatChem, 2014, 6, 1438.

11 K.M. Kang, H.W. Kim, I.W. Shim, H.Y. Kwak, Fuel Process. Technol. 2011, 92, 1236; X. Du, D. Zhang, R. Gao, L. Huang, L. Shi, J. Zhang, Chem. Commun. 2013, 49, 6770; T. Wu, W. Cai, P. Zhang, X. Song, L. Gao, RSC Adv. 2013, 3, 23976.

12 M.S. Aw, I.G. Osojnik Črnivec, A. Pintar, Catal. Sci. Tech. 2014, 4, 1340.

13 M.S. Aw, M. Zorko, P. Djinović, A. Pintar, Appl. Catal. B 2015, 164, 100.

14 Q. Yuan, A.X. Yin, C. Luo, L.D. Sun, Y.W. Zhang, W.T. Duan, H.C. Liu, C.H. Yan, J. Am. Chem. Soc. 2008, 130, 3465.

15 I.E. Wachs, Catal. Today 2005, 100, 79; Z. Yan, M. Cai, P.K. Shen, Sci. Rep. 2013, 3, 1646; I.E. Wachs, T. Kim, E.I. Ross, Catal. Today 2006, 116, 162.

16 P.B. Lihitkar, S. Violet, M. Shirolkar, J. Singh, O.N. Srivastava, R.H. Naik, S.K. Kulkarni, Mater. Chem. Phys. 2012, 133, 850; Q. Wu, F. Zhang, J. Yang, Q. Li, B. Tu, D. Zhao, Micropor. Mesopor. Mater. 2011, 143, 406; M. Boutros, M.E. Gálvez, T. Onfroy, P.D. Costa, Micropor. Mesopor. Mater. 2014, 183, 1.

17 L. Salvati, L.E. Makovsky, J.M. Stencel, F.R. Brown, D.M. Hercules, J. Phys. Chem. 1981, 85, 3700.

18 L. Xu, Z. Miao, H. Song, W. Chen, L. Chou, Catal. Sci. Technol. 2014, 4, 1759.

19 W. Schmidt, Microporous Mesoporous Mater. 2009, 117, 372.

20 M. Gaudon, L.C. Robertson, E. Lataste, M. Duttine, M. Ménétrier, A. Demourgues, Ceram. Int. 2014, 40, 5201.

21 J. Gurgul, K. Łątka, I. Hnat, J. Rynkowski, S. Dzwigaj, Microporous Mesoporous Mater. 2013, 168, 1.

22 P. Djinović, I.G. Osojnik Črnivec, B. Erjavec, A. Pintar, Appl. Catal. B 2012, 125, 259.

23 D. San-José-Alonso, J. Juan-Juan, M.J. Illán-Gómez, M.C. Román-Martínez, Appl. Catal. A 2009, 371, 54.

24 L. Ji, S. Tang, H.C. Zeng, J. Lin, K.L Tan, Appl. Catal. A 2001, 207, 247; T. Shishido, M. Sukenobu, H. Morioka, R. Furukawa, H. Shirahase, K. Takehira, Catal. Letters 2001, 73, 21.

25 A.B. Anderson, J.J. Maloney, J. Phys. Chem. 1988, 92, 809.

26 S. Chianese, J. Loipersböck, M. Malits, R. Rauch, H. Hofbauer, A. Molino, D. Musmarra, Fuel Process. Technol. 2015, 132, 39.

27 T.C. Xiao, A. Hanif, A.P.E. York, M.L.H. Green, Catal. Today 2009, 147, 196.

28 M.M. Makri, M.A. Vasiliades, K.C. Petallidou, A.M. Efstathiou, Catal. Today 2016, 259, 150.

29 A. Kubacka, R. Si, P. Michorczyk, A. Martínez-Arias, W. Xu, J.C. Hanson, J.A. Rodriguez, M. Fernández-García, Appl. Catal. B 2013, 132, 423.

30 M. O'Connell, G. Kolb, R. Zapf, Y. Men, V. Hessel, Catal. Today 2009, 144, 306.